Energy-aware 3D Leader-Follower Flight Trajectory Optimization for Fixed-Wing Aircraft

Praveen K. Ranjan*, Johnathan Votion† and Yongcan Cao‡
University of Texas at San Antonio, San Antonio, TX, 78249

Dzung Tran§, David Casbeer¶, and Isaac Weintraub‖
U.S. Air Force Research Laboratory, Wright-Patterson Air Force Base, OH 45433.

This paper focuses on optimizing the 3D flight trajectory of a fixed-wing aircraft when performing wingman maneuvers in a leader-follower formation scenario. Instead of a rigid formation position, the desired formation is defined as set of points configured as a ring structure located behind the leader when both the leader and the wingman aircraft are modeled by high order dynamics. In particular, we formulate the optimization problem under three different system structures: (i) naturally constrained, (ii) ring angle constrained and (iii) controller constrained. These system structures reflect the variation of inputs to the system under different levels of control freedom, from an unknown control structure to a known control structure. The optimization objective is to minimize the thrust profile so that the follower can minimize its consumed energy to achieve the desired wingman maneuver. Our simulation studies demonstrate that optimized solutions are attainable for all three cases. Moreover, for a naturally constrained system, there exists a convergent steady-state solution for the wingman's position along the ring structure that represents a global solution, regardless of the wingman's initial states.

I. Introduction

Formation control in UAV applications has been used to, e.g., provide sensor coverage [1], form communication networks [2], and conserve energy during travel [3]. The research in recent works surrounding formation control is found to involve topics regarding particle swarm implementation, potential field methods, and system control under sensor constraints (*e.g.*, communication delays, measurement noise, etc.). For example, in [4], a combination of robust and PID control is used to provide a small group of fixed-wing UAVs the capability to effectively strike a target. Their proposed controller is proven asymptotically stable and can resist wind fields while performing precise air strikes on a ground target. In [5], a UAV is commanded to land on a moving UGV by orienting a virtual 'line' that links the UAV with the UGV. The UAV is commanded to fly directly over the UGV to orient the virtual line to be vertically straight, and maintain a straight line while lowering its altitude to land. In [6], a guidance control based on the backstepping approach is proposed with stability proven via the Lyapunov function. The formation is a triangle shape with a virtual leader positioned at the center of the shape and followers positioned at the triangle's vertices. Complex wind fields are also considered in their work. In [7], an artificial potential field is constructed using the communication topology and communication weights. A Null space behavior approach is designed to fuse obstacle avoidance with formation keeping, and combine them into a single command. Their formation keeping control is designed as a second order consensus control algorithm. In [8], the UAV models are represented using point mass models, and the autopilots are based on a first-order system. They utilize a potential field based control that enables the group of UAVs to converge to the desired formation. By combining the artificial potential field method with a formation division method a flexible formation is achieved for congested settings. In [9], the formation is specified as three UAVs in triangle formation. A virtual leader is used to determine the flight trajectory where a potential field is applied to the virtual leader in order to track the target. Repulsive forces are used to prevent collision and distribute the followers. The collision avoidance trajectory is the

*Graduate Student, Department of Electrical and Computer Engineering.
†Postdoctoral Research Fellow, Department of Electrical and Computer Engineering.
‡Assistant Professor, Department of Electrical and Computer Engineering.
§Research Associate, Control Science Center of Excellence.
¶Team Lead, Control Science Center of Excellence.
‖Research Engineer, Control Science Center of Excellence.

result of a superposition function taken with respect to two rotation potential field vectors. The work in [10] proposes a collision avoidance algorithm based on bi-directional network connection structure. A consensus based algorithm and leader-follower controller are simultaneously applied to provide a convergent formation control. The consensus based collision avoidance algorithm is based on an improved artificial potential field method and includes obstacle avoidance. In [11], the desired UAV path is parameterized as a Pythagorean Hodograph and decomposes particle swarm optimization (PSO) solutions into 'subswarms'. The subswarms communicate with each other to form cooperative groups that update the best known locations in the optimal direction. This improved PSO is extended in [12]. The work in [12] proposes a path planning algorithm for UAV formation based on comprehensively improved PSO. A chaos based logistic map is used to improve the particle initial distribution and adaptive linear-varying variables are used to represent the constant acceleration coefficients and maximum velocity. In addition a mutation strategy is used for replacing the undesired particles with desired ones. Their proposed PSO is theoretically shown to speed up convergence and improve solution optimality. In [13], a formation control based on the second order consensus is developed that generates steering commands. In their algorithm a cooperative guidance algorithm and cooperative control algorithm work together to control the position and attitude, respectively. The full-state closed-loop control strategy provides desired acceleration, pitch rate, and heading rate. 'Synchronization' technology referred to their work is synonymous with consensus control, and is used to overcome measurement error. To handle disturbances and uncertainties, the authors in [14] propose an adaptive model predictive control with extended state observers. The extended state observer estimates the disturbance and is ultimately bounded, allowing for the design of a distributed trajectory tracking controller with disturbance rejection. Their work adopts a flexible virtual structure for defining the formation. In [15] the mathematical model for a quadcopter UAV is partitioned into two subsystems, linear-attitude control and non-linear position control, where state information is obtained through communication with local neighbors. To control the thrust a backstepping outer position controller interfaces with the inner attitude controller in a cascaded control structure. A Lyapunov-Krasovskii approach is used to prove stability with considerations made for communication time delays. In [16], a cooperative relative localization method is proposed for UAVs operating in GPS denied environments. Ultra-wideband Ranging and Communication Network is utilized to both sense the inter-UAV distances and exchange information. A continuous double integrator model is considered for formation control using a discrete controller. They propose a discrete-time controller involving the localization estimates and measurement noises by discretizing a referenced control algorithm.

One principle formation control problem is the leader-follower tracking problem, whose objective is to derive control algorithms such that the follower can track the leader in a specific formation setting. In [17], a leader-follower feedback formation control is developed, where the follower only uses the distance and bearing angle to the leader as feedback. Constraints are provided on the leader such that the follower can maintain formation. The controller is based on a turning rate controller for the follower to track the leader and a velocity controller that uses the bearing angle. The policy for the turning rate uses two curved sliding surfaces, which are composed of piecewise linear segments. The resulting behavior of the follower is that it orbits around a stationary target and is capable of tracking a moving target. In other works, close proximity formations are used to obtain efficient flight dynamics. Drag reduction is achieved by having the wingman follow the leader's flight path in close proximity. In [18], a PI autopilot control is designed that uses a mix of separation errors and maneuver errors. The controller is an extension of the heading-hold and mach-hold autopilots, but is implemented by involving two flight vehicles and their accurate positions. The position of the leader relative to the wingman is assumed available and the aircrafts are modeled using first-order dynamics. The work in [18] is extended in [19] to include the aerodynamic effects of flying tight formations to achieve a reduction in the formation's induced drag. One important formation setting is the virtual structure method. In the virtual structure method, the trajectories of the system agents are modeled by the movement of a structure through a space. The controller is developed by defining the dynamics of the virtual structure, then translating those dynamics to define the path of the followers. A virtual structure can be categorized as either rigid or flexible. A rigid virtual structure generates agent trajectories by maintaining fixed distances between agents within the formation, but the rigid virtual structure can result in deformations of the planned trajectories due to nonholonomic constraints of the system vehicles. In [20–24], the deformation problem is solved by utilizing a flexible virtual structure, where the formation constraints can be loosely applied to provide smooth turning conditions. In [24], the flexibility of the wingman's formation position is constrained to a ring structure located a certain distance behind the leader. Two control algorithms are proposed: an explicit control defines a point along the ring and changes depending on the current position of the follower, and a potential field method.

In this paper, we focus on optimizing control strategies to enable 3D leader-follower formation maneuvers for fixed-wing aircraft such that the wingman aircraft can minimize its thrust usage while staying in the desired formation with the leader. Since the thrust is proportional to the energy consumed by the wingman, minimizing the thrust means the minimization of energy consumption of the wingman. In the context of this paper, a 6-DOF model is chosen to

represent the aircraft dynamics. Moreover, the designed control strategies are only for the wingman as the leader's trajectory is given, indicating that the control input for the leader is pre-determined. To focus on the optimization aspect, this paper does not investigate the impact of communication between the leader and the wingman. Instead, we assume that the wingman has full knowledge of the leader without relying on a communication channel. In addition, measurement noise and wind disturbance are neglected. By neglecting communication and sensing models, we simplify the problem to be more focused on the analytical and optimization aspects for controlling the 6-DOF model in a leader-follower framework. Following the work in [24], we adopt the ring structure formation for the energy saving aspects as it reflects the aerodynamic benefits obtained by flying in the wake of the leader's flight path. Based on the 'explicit' ring structure approach, we show that improved thrust profiles are obtainable, which is possible by modifying the saturation bounds that are applied to the wingman's direct control inputs.

II. Preliminaries

This section introduces the mathematical background for the leader-follower tracking problem using a ring structure to define the desired formation position. We extend the ring formation controller developed in [24] by incorporating analytical expressions for the system variables. The analytical calculation replaces the previously used *command* filters that were used to compute the second derivative needed for control feedback. The original model in [24] has also been improved by modelling the aerodynamic drag. This improvement allows us to generate more practical trajectories and determine the forces used in energy calculations.

A. System Kinematics

A point-mass aircraft model for three-dimensional flight over a flat, non-rotating earth is used as the kinematic model for the fixed-wing unmanned aerial vehicles [25]. With the assumption of thrust along the forward path of the vehicle, the aircraft model is defined as

$$\begin{aligned}
\dot{x}_i(t) &= V_i(t)\cos\gamma_i(t)\cos\chi_i(t),\\
\dot{y}_i(t) &= V_i(t)\cos\gamma_i(t)\sin\chi_i(t),\\
\dot{h}_i(t) &= V_i(t)\sin\gamma_i(t),\\
\dot{V}_i(t) &= \frac{T_i(t)-D_i(t)}{m_i} - g\sin\gamma_i(t),\\
\dot{\gamma}_i(t) &= \frac{g}{V_i(t)}(n_i(t)\cos\phi_i(t)-\cos\gamma_i(t)),\\
\dot{\chi}_i(t) &= \frac{g}{V_i(t)}\frac{n_i(t)\sin\phi_i(t)}{\cos\gamma_i(t)},
\end{aligned} \tag{1}$$

for $i \in \{l, w\}$, with airspeeds $V_i(t) \in \mathbb{R}_{>0}$, thrust $T_i(t)$, aerodynamic drag $D_i(t)$, mass $m_i \in \mathbb{R}_{>0}$, acceleration due to gravity g, flight path angle $\gamma_i(t)$, heading angle $\chi_i(t)$, load factor $n_i(t)$, and bank angle $\phi_i(t)$, where l denotes the leader and w denotes the wingman. This formulation can handle thrust reversal as well as the effect of speed brakes, if these capabilities are available. Note that the system bank angles $\phi_i(t)$, load factors $n_i(t)$ and thrusts $T_i(t)$ are the input variables. By differentiating $\dot{x}_i(t)$, $\dot{y}_i(t)$ and $\dot{h}_i(t)$ and substituting in the dynamics for $V_i(t)$, $\gamma_i(t)$ and $\chi_i(t)$ we obtain a new form of the model given as

$$\begin{aligned}
\ddot{x}_i(t) &= u_{i1}(t),\\
\ddot{y}_i(t) &= u_{i2}(t),\\
\ddot{h}_i(t) &= u_{i3}(t),
\end{aligned} \tag{2}$$

where $u_i(t) = [u_{i1}(t), u_{i2}(t), u_{i3}(t)]'$ are the new control variables. Each aircraft can be modelled using three state variables $[V_i, \gamma_i, \chi_i]^T$ and controlled using three control inputs $[T_i, n_i, \phi_i]^T$ or $[u_{i1}, u_{i2}, u_{i3}]^T$. For the formation control problem vehicle position is also required to be added to the vehicle state. So, the vehicle state is represented by $[x_i, y_i, h_i, V_i, \gamma_i, \chi_i]^T$ with (1) representing the state derivatives. The relationship between the control u_i and the

variables ϕ_i, n_i and T_i is defined as

$$\begin{aligned}
\phi_i &= \arctan\left(\frac{u_{i2}\cos\chi_i - u_{i1}\sin\chi_i}{\cos\gamma_i(u_{i3}+g) - \sin\gamma_i(u_{i1}\cos\chi_i + u_{i2}\sin\chi_i)}\right),\\
n_i &= \frac{\cos\gamma_i(u_{i3}+g) - \sin\gamma_i(u_{i1}\cos\chi_i + u_{i2}\sin\chi_i)}{g\cos\phi_i},\\
T_i &= (\sin\gamma_i(u_{i3}+g) + \cos\gamma_i(u_{i1}\cos\chi_i + u_{i2}\sin\chi_i))m_i + D_i.
\end{aligned} \tag{3}$$

Furthermore, the drag D_i is estimated from the drag polar as

$$D_i = \rho {V_i}^2 A_i (C_{d_{0_i}} + C_{d_{ind}}), \tag{4}$$

with the *parasitic* drag coefficient $C_{d_{0_i}}$ and the *induced* drag coefficient $C_{d_{ind}}$ defined as [26]

$$\begin{aligned}
C_{d_{ind}} &= \frac{C_{l_i}^2}{\pi A_R e},\\
C_{l_i} &= \frac{2n_i m_i g}{\rho {V_i}^2 A_i},
\end{aligned} \tag{5}$$

where A_R is the wing aspect ratio, A_i is the surface area of the wings, ρ is the air density, n_i is the load factor, m is the mass, g is the gravity, and e is the Oswald's efficiency parameter. Next, we define the dynamics for the wingman's tracking error with respect to an arbitrary position along a ring structure located behind the leader.

B. Tracking Error

Consider the system dynamics given by

$$\begin{aligned}
\dot{r}_i(t) &= v_i(t),\\
\dot{v}_i(t) &= u_i(t),
\end{aligned} \tag{6}$$

where $r_i(t) = [x_i(t), y_i(t), h_i(t)]'$ is the position of the ith vehicle, $v_i(t) = [\dot{x}_i(t), \dot{y}_i(t), \dot{h}_i(t)]'$ is the velocity, and $u_i \in \mathbb{R}^3$ is the control input. A desired formation is one where the follower is able to maintain its position along a rigid ring structure located behind the leader. The ring structure is a set of points in the $y_l z_l$ plane arranged in a circular formation with radius R around the point C. The points along the ring structure are defined using a set of vectors Γ. Let $r_l^* \in \Gamma$ represent the displacement vector associated with the desired position along the ring structure. The displacement vector is defined as

$$r_l^* = \begin{bmatrix} C_x \\ C_y + R\cos\varphi(t) \\ C_z - R\sin\varphi(t) \end{bmatrix}, \tag{7}$$

where $C = [C_x, C_y, C_z]'$ is a vector representing the center of the ring, R is the radius of the ring, and $\varphi(t) \in (-\pi, \pi)$ is the ring angle taken counterclockwise from the $+y_l$ axis in the $y_l z_l$ plane. Figure 1 shows a diagram of the the ring structure.

The desired position is calculated as the displacement vector rotated into the inertial frame and displaced by the leader's position. Let $\mathcal{R}_l^i(\gamma_l, \chi_l)$ represent the rotation matrix for the transformation from the leader frame to the inertial frame, defined as $\mathcal{R}_l^i(\gamma_l, \chi_l) = \mathcal{R}_1(\chi_l)\mathcal{R}_2(\gamma_l)$, where

$$\mathcal{R}_1(\chi_l) = \begin{bmatrix} \cos\chi_l & -\sin\chi_l & 0 \\ \sin\chi_l & \cos\chi_l & 0 \\ 0 & 0 & 1 \end{bmatrix}, \tag{8}$$

and

$$\mathcal{R}_2(\gamma_l) = \begin{bmatrix} \cos\gamma_l & 0 & \sin\gamma_l \\ 0 & 1 & 0 \\ -\sin\gamma_l & 0 & \cos\gamma_l \end{bmatrix}. \tag{9}$$

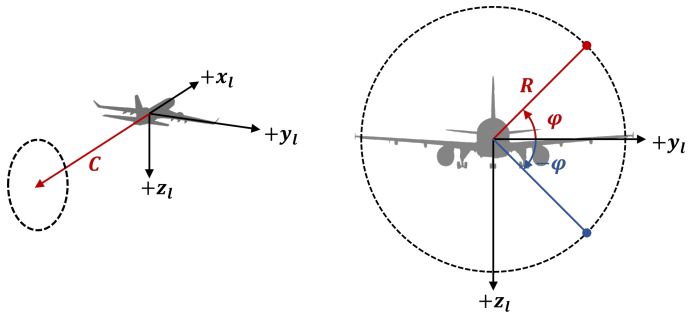

Fig. 1 A diagram showing the ring structure with respect to the leader's vehicle frame. The leader is shown as the grey vehicle with $x_l y_l z_l$ vehicle frame axes. This particular configuration reflects a C vector where $|C_x| < 0$ and $C_y = C_z = 0$. Hence, the center of the ring structure is positioned directly behind the leader. The ring structure is formed by a set of position vectors Γ. The vectors Γ are defined in terms of the center C, radius R and ring angle $\varphi \in (-\pi, \pi)$. The ring angle φ is taken counterclockwise from the $+y_l$ axis in the $y_l z_l$ plane.

Let $r_d(t)$ represent the desired position in the inertial frame, and be defined as

$$r_d(t) = r_l(t) + \mathcal{R}_l^i(t) r_l^*(t). \tag{10}$$

From equations (1)-(10) we obtain the error dynamics

$$\begin{aligned} e(t) &= r_f(t) - r_l(t) - \mathcal{R}_l^i(t) r_l^*(t), \\ \dot{e}(t) &= v_f(t) - v_l(t) - \frac{d}{dt}[\mathcal{R}_l^i(t) r_l^*(t)], \\ \ddot{e}(t) &= u_f(t) - u_l(t) - \frac{d^2}{dt^2}[\mathcal{R}_l^i(t) r_l^*(t)]. \end{aligned} \tag{11}$$

We now solve for the differential terms of the rotated vector $\mathcal{R}_l^i(t) r_l^*(t)$ used within (11). The first derivative of the rotated vector is given as

$$\frac{d}{dt}[\mathcal{R}_l^i(t) r_l^*(t)] = \dot{\mathcal{R}}_l^i(t) r_l^*(t) + \mathcal{R}_l^i(t) \dot{r}_l^*(t). \tag{12}$$

Computing the first derivative of the displacement vector gives

$$\dot{r}_l^*(t) = \begin{bmatrix} 0 \\ -R\sin\varphi(t) \\ -R\cos\varphi(t) \end{bmatrix} \dot{\varphi}(t). \tag{13}$$

Computing the first derivative of the rotation matrix gives

$$\dot{\mathcal{R}}_l^i = \dot{\mathcal{R}}_1 \mathcal{R}_2 + \mathcal{R}_1 \dot{\mathcal{R}}_2, \tag{14}$$

where

$$\begin{aligned} \dot{\mathcal{R}}_1 &= \frac{\partial \mathcal{R}_1(\chi_l)}{\partial \chi_l} \dot{\chi}_l(t) \\ &= \begin{bmatrix} -\sin\chi_l & -\cos\chi_l & 0 \\ \cos\chi_l & -\sin\chi_l & 0 \\ 0 & 0 & 0 \end{bmatrix} \dot{\chi}_l(t), \end{aligned} \tag{15}$$

$$\begin{aligned} \dot{\mathcal{R}}_2 &= \frac{\partial \mathcal{R}_2(\gamma_l)}{\partial \gamma_l} \dot{\gamma}_l(t) \\ &= \begin{bmatrix} -\sin\gamma_l & 0 & \cos\gamma_l \\ 0 & 0 & 0 \\ -\cos\gamma_l & 0 & -\sin\gamma_l \end{bmatrix} \dot{\gamma}_l(t), \end{aligned} \tag{16}$$

$\dot{\chi}_l$ and $\dot{\gamma}_l$ are given in (1), and $\mathcal{R}_1$ and $\mathcal{R}_2$ are given in (8) and (9), respectively.

The second derivative of the rotated vector is given as

$$\begin{aligned}\frac{d^2}{dt^2}[\mathcal{R}_l^i(t)r_l^*(t)] &= \frac{d}{dt}[\dot{\mathcal{R}}_l^i(t)r_l^*(t)] + \frac{d}{dt}[\mathcal{R}_l^i(t)\dot{r}_l^*(t)], \\ &= \ddot{\mathcal{R}}_l^i(t)r_l^*(t) + \dot{\mathcal{R}}_l^i(t)\dot{r}_l^*(t) + \dot{\mathcal{R}}_l^i(t)\dot{r}_l^*(t) + \mathcal{R}_l^i(t)\ddot{r}_l^*(t).\end{aligned} \tag{17}$$

Computing the second derivative of the displacement vector gives

$$\ddot{r}_l^*(t) = \begin{bmatrix} 0 \\ -R\cos\varphi(t) \\ R\sin\varphi(t) \end{bmatrix} \dot{\varphi}^2(t) + \begin{bmatrix} 0 \\ -R\sin\varphi(t) \\ -R\cos\varphi(t) \end{bmatrix} \ddot{\varphi}(t). \tag{18}$$

Computing the second derivative of the rotation matrix gives

$$\ddot{\mathcal{R}}_l^i = \ddot{\mathcal{R}}_1\mathcal{R}_2 + \dot{\mathcal{R}}_1\dot{\mathcal{R}}_2 + \dot{\mathcal{R}}_1\dot{\mathcal{R}}_2 + \mathcal{R}_1\ddot{\mathcal{R}}_2, \tag{19}$$

where

$$\begin{aligned}\ddot{\mathcal{R}}_1 &= \frac{d}{dt}\left[\frac{\partial\mathcal{R}_1(\chi_l)}{\partial\chi_l}\right]\dot{\chi}_l(t) + \frac{\partial\mathcal{R}_1(\chi_l)}{\partial\chi_l}\frac{d}{dt}[\dot{\chi}_l(t)] \\ &= \begin{bmatrix} -\cos\chi_l & \sin\chi_l & 0 \\ -\sin\chi_l & -\cos\chi_l & 0 \\ 0 & 0 & 0 \end{bmatrix}\dot{\chi}_l^2(t) + \frac{\partial\mathcal{R}_1(\chi_l)}{\partial\chi_l}\ddot{\chi}_l(t),\end{aligned} \tag{20}$$

and

$$\begin{aligned}\ddot{\mathcal{R}}_2 &= \frac{d}{dt}\left[\frac{\partial\mathcal{R}_2(\gamma_l)}{\partial\gamma_l}\right]\dot{\gamma}_l(t) + \frac{\partial\mathcal{R}_2(\gamma_l)}{\partial\gamma_l}\frac{d}{dt}[\dot{\gamma}_l(t)] \\ &= \begin{bmatrix} -\cos\gamma_l & 0 & -\sin\gamma_l \\ 0 & 0 & 0 \\ \sin\gamma_l & 0 & -\cos\gamma_l \end{bmatrix}\dot{\gamma}_l^2(t) + \frac{\partial\mathcal{R}_2(\gamma_l)}{\partial\gamma_l}\ddot{\gamma}_l(t).\end{aligned} \tag{21}$$

The terms ${\dot{\chi}_l}^2$ and ${\dot{\gamma}_l}^2$ are calculated via (1). The terms $\frac{\partial\mathcal{R}_1(\chi_l)}{\partial\chi_l}$ and $\frac{\partial\mathcal{R}_2(\gamma_l)}{\partial\gamma_l}$ are extracted from (15) and (16), respectively. Given the model in (1), we assume that the rotational forces (*i.e.*, torque) on the vehicles are very small. Hence, we approximate the angular accelerations as $\ddot{\chi}_l(t) \approx 0$ and $\ddot{\gamma}_l(t) \approx 0$, which allows us to forgo developing the analytical expressions for these terms as well as the assumption that we have access to this information.

III. Flight Trajectory Optimization

In this section, we focus on developing optimized control strategies for the wingman such that it can minimize its thrust usage while staying in the desired formation with the leader. Minimization of the thrust also means the minimization of energy usage for the wingman. Under normal operating conditions for fixed-wing flight, there is a trade-off between thrust minimization and tracking performance. In other words, the system's performance will depend on how the constraints and inputs are defined. Therefore, we investigate the optimized solutions for three cases and structure them differently by changing the system's input variables. In the first case, namely, case A, we initially relax the optimization constraints by defining the inputs of the system to be the wingman inputs $\{T_w, n_w, \phi_w\}$ and the ring angle $\varphi(t)$, which leads to an optimized solution where the thrust profile is erratic. To smooth the thrust profile, the control inputs are transferred to be the wingman input rates $\{\dot{T}_w, \dot{n}_w, \dot{\phi}_w\}$ and ring angle acceleration rate $\ddot{\varphi}(t)$. In the second case, namely, case B, we utilize the same wingman input rates as in case A, *i.e.* $\{\dot{T}_w, \dot{n}_w, \dot{\phi}_w\}$, but we remove the ring angle acceleration rate $\ddot{\varphi}(t)$ from the controllable parameters. Instead, the ring angle $\varphi(t)$ and ring angle rate $\dot{\varphi}(t)$ are determined by the wingman's position, making the ring angle be constrained by the coupled dynamics of the leader and the wingman. In the third case, namely, case C, a controller is implemented that uses the dynamics of the wingman's desired position and leader controls as feedback. With this feedback, the system is ultimately reduced to having a single input variable that is the ring angle acceleration rate $\ddot{\varphi}(t)$. Additionally, a description of the procedure for obtaining the initial *guess* data used for initializing the optimizer is also included at the end of this section.

A. Case A: Optimization with Kinematic Constraints

Let the aircraft's states be represented by the vector $[x_i, y_i, h_i, V_i, \gamma_i, \chi_i]'$ for $i \in \{l, w\}$. Let $r_w(t) = [x_w, y_w, h_w]' \in \mathbf{z}_w(t)$ represent the position of a wingman in the inertial frame. There exists a desired wingman position $r_d(t) = [x_d, y_d, h_d]'$ in the inertial frame, defined in a rigid structure formation and determined by the orientation of the leader. The trajectory $r_d(t)$ may not be feasible due to the kinematic limitations of the wingman. Therefore, a desired trajectory $r_w^*(t)$ is defined that represents the feasible trajectory of the wingman. Assuming that $\mathbf{z}_l(t)$ is known in the duration $t \in [t_o, t_f]$, our objective is to compute the feasible trajectory $r_w^*(t)$ that minimizes the thrust T_w of the wingman using a smooth thrust profile while adding a constraint that $\left|\left|r_d(t) - r_w^*(t)\right|\right|$ is within some threshold. Here, we form a set of optimization problems that structures the leader-follower ring structure formation problem with the constraints needed to find controls $\{T_w(t), n_w(t), \phi_w(t)\}$ that generate $r_w^*(t)$. In case A, the wingman input rates $\{\dot{T}_w, \dot{n}_w, \dot{\phi}_w\}$ and ring angle acceleration rate $\ddot{\varphi}(t)$ are used as inputs to the optimized system. For the case A structure, the state vector z_{opt}, control vector u_{opt}, and differential state vector $\dot{z}_{opt}$ are defined as

$$z_{opt} = [z_w, T_w, n_w, \phi_w, \varphi, \dot{\varphi}] \in \mathbb{R}^{11x1}, \tag{22}$$

$$u_{opt} = [\dot{T}_w, \dot{n}_w, \dot{\phi}_w, \ddot{\varphi}] \in \mathbb{R}^{4x1}, \tag{23}$$

$$\dot{z}_{opt} = [\dot{z}_w, \dot{T}_w, \dot{n}_w, \dot{\phi}_w, \dot{\varphi}, \ddot{\varphi}] \in \mathbb{R}^{11x1}. \tag{24}$$

The optimization problem for case A is given as

$$\begin{aligned}
&\min_{\dot{\phi}_w(t), \dot{n}_w(t), \dot{T}_w(t), \ddot{\varphi}(t)} \int_{t_o}^{t_f} T_w(\tau) d\tau, \\
\text{s.t.} \quad & ||r_d(t) - r_w^*(t)|| \leq \alpha, \\
& 0 < T_w \leq 800, \\
& -0 < n_w < 2, \\
& -\pi/3 < \phi_w < \pi/3, \\
& -10 < \dot{T}_w \leq 10, \\
& -0.05 < \dot{n}_w \leq 0.05, \\
& -0.05 < \dot{\phi}_w \leq 0.05, \\
& -0.1 < \ddot{\varphi} < 0.1,
\end{aligned} \tag{25}$$

subject to (24). The cost function used in (25) is the integration of the wingman's thrust $T_w(t)$ over the flight time. Recall that $\dot{T}_w$ is used as a control parameter. This term is constrained within the optimization algorithm to ensure that a smooth thrust profile is obtained. Note that we also include T_f, n_f, ϕ_f in the optimization state. This can allow for explicit bounds to be placed in their operating range, hence preventing the inputs from converging to infeasible values while also ensuring a practical range of values. In case A, we determine the desired position on the ring through control of $\ddot{\varphi}$. In the next case, case B, we describe the optimization problem where the desired position is no longer controlled. Instead, it is predefined according to the wingman's position.

B. Case B: Optimization with Ring Angle Constraint

In case A, the desired position is free to move along the ring structure. Hence, the optimizer has the freedom to choose the desired position that aids the solution search to obtain a smooth and minimal thrust profile. In case B, the ring angle variable is redefined using the wingman's state information as feedback. The ring angle is defined as the angle taken with respect to the intersecting position of the ring structure and a LOS vector between the wingman and the center of the ring structure, given as

$$\varphi = \arctan\left(\frac{C_z^l - z_w^l}{C_y^l - y_w^l}\right), \tag{26}$$

where $\{C_y^l, C_z^l\}$ is $\{C_y, C_z\} \in C$ rotated into the leader's vehicle frame and $\{y_w^l, z_w^l\}$ is the wingman's $\{y_w, z_w\}$ coordinate rotated into the leader's vehicle frame. The ring angle dynamics is determined by the movement of the leader and the follower. Following [24], given (1) and (26), the dynamics for the angle on the ring is defined as

$$\dot{\varphi} = \frac{1}{d}(\dot{y}_w^l(t) \sin\varphi - \dot{z}_w^l(t) \cos\varphi), \qquad \varphi(t_o) = \varphi_o, \tag{27}$$

where $\dot{y}^l_w(t)$ and $\dot{z}^l_w(t)$ are the differential terms for the y and z components of the wingman's position taken with respect to the leader's vehicle frame, and $1/d$ (=0.5) represents the formation angle gain. Figure 2 shows a diagram depicting the configuration of the desired position using the new definition of the ring angle.

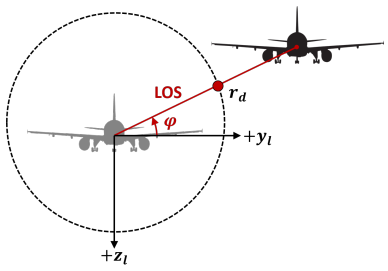

Fig. 2 A diagram in the leader's $y_l z_l$ frame showing the ring angle φ taken with respect to the intersecting position r_d of the ring structure and a LOS vector between the wingman and the center of the ring structure.

The state vector z_{opt}, control vector u_{opt} and differential state vector $\dot{z}_{opt}$ for the case B optimization problem are defined as

$$z_{opt} = [z_w, T_w, n_w, \phi_w, \varphi] \in \mathbb{R}^{10x1}, \tag{28}$$

$$u_{opt} = [\dot{T}_w, \dot{n}_w, \dot{\phi}_w] \in \mathbb{R}^{3x1}, \tag{29}$$

$$\dot{z}_{opt} = [\dot{z}_w, \dot{T}_w, \dot{n}_w, \dot{\phi}_w, \dot{\varphi}] \in \mathbb{R}^{10x1}. \tag{30}$$

The state differential vector shown in (30) utilizes (27) to describe the dynamics for the angle on the ring. By redefining the ring angle in terms of the wingman's position and dynamics, the ring angle is no longer treated as a controlled variable and the optimization problem for a known trajectory of $\mathbf{z}_l(t)$ in the duration of time $t \in [t_o, t_f]$ is described by

$$\begin{aligned} \min_{\dot{\phi}_w(t), \dot{n}_w(t), \dot{T}_w(t)} & \int_{t_o}^{t_f} T_w(\tau) d\tau, \\ \text{s.t.} \quad & ||r_d(t) - r^*_w(t)|| \leq \alpha, \\ & 0 < T_w \leq 800, \\ & -0 < n_w < 2, \\ & -\pi/3 < \phi_w < \pi/3, \\ & -10 < \dot{T}_w \leq 10, \\ & -0.05 < \dot{n}_w \leq 0.05, \\ & -0.05 < \dot{\phi}_w \leq 0.05, \end{aligned} \tag{31}$$

subject to (30), where $||\cdot||$ is the euclidean norm and α is some maximum threshold. The case B path constraint and variable bounds are also included in (31).

C. Case C: Optimization with Controller Constraint

For case C, instead of substituting in an alternative definition for the ring angle control, the definition for the wingman's controls are substituted with a designed controller instead. This restricts the optimization's gradient search and reduces the system's input variables to be only the ring angle information. Via utilizing the ring angle dynamics, we can control the ring angle and ring angle rate through the ring angle acceleration $\ddot{\varphi}(t)$. Let $u_d(t) = [u_{d1}, u_{d2}, u_{d3}]'$ represent the designed controller and $u(t) \in \mathbb{R}^3$ be the saturated control signal defined as

$$u(t) = \text{sat}(u_d) = \begin{bmatrix} \text{sgn}(u_{d1}) \min(|u_{d1}|, \bar{u}_1) \\ \text{sgn}(u_{d2}) \min(|u_{d2}|, \bar{u}_2) \\ \text{sgn}(u_{d3}) \min(|u_{d3}|, \bar{u}_3) \end{bmatrix}, \tag{32}$$

where $\bar{u} = [\bar{u}_1, \bar{u}_2, \bar{u}_3]'$ is the saturation constraint. Let a new variable $s(t)$ be defined as

$$s(t) = \dot{e}(t) + k_1 e(t) + \xi(t), \tag{33}$$

where

$$\dot{\xi}(t) = -k_2\xi(t) + \Delta u(t), \qquad \xi(0) = \xi_o, \tag{34}$$

and

$$\Delta u(t) = u_d(t) - u(t). \tag{35}$$

The desired control $u_d(t)$ is defined as

$$u_d(t) = u_l(t) + \frac{d^2}{dt^2}[\mathcal{R}_l^i(t) r_l^*(t)] - k_1\dot{e}(t) + k_2\xi(t) - k_3 s(t) - e(t). \tag{36}$$

Using the 'explicit' ring structure approach from [24], we can obtain improved thrust profiles by modifying the saturation bounds to be applied to the wingman's thrust, load factor, and bank angle controls. The controller developed in [24] bounds the wingman's xyz accelerations as shown in (32). Differently, we map the accelerations to the wingman's controls, and then apply the saturation bounds because our analysis of the 'explicit' control algorithm showed that the wingman uses a negative thrust to slow down in certain parts of the trajectories. This is impractical since thrust can only be positive and the aircraft relies on drag to slow down. Saturating $[T_w, n_w, \phi_w]'$ instead of $[\ddot{x}_w, \ddot{z}_w, \ddot{h}_w]'$ after the analytical conversion from $[\ddot{x}_w, \ddot{z}_w, \ddot{h}_w]'$ to $[T_w, n_w, \phi_w]'$ via (3) helps to ensure the wingman's control inputs are nonnegative and hence practical. Let $[\check{T}_w, \check{n}_w, \check{\phi}_w]'$ represent the saturated values of the wingman controls. We define the saturated wingman controls as

$$\begin{bmatrix} \check{T}_d \\ \check{n}_d \\ \check{\phi}_d \end{bmatrix} = \text{sat}\left(\begin{bmatrix} T_d \\ n_d \\ \phi_d \end{bmatrix}\right) = \begin{bmatrix} \max(0, \min(|T_d|, \bar{T}_d)) \\ \max(0, \min(|n_d|, \bar{n}_d)) \\ \text{sgn}(\phi_d)\min(|\phi_d|, \bar{\phi}_d) \end{bmatrix}, \tag{37}$$

where $[\bar{T}_w, \bar{n}_w, \bar{\phi}_w]'$ is the saturation constraint. Now we can convert the saturated control inputs to accelerations $u(t)$ via

$$\begin{aligned} u_1(t) &= \frac{\check{T}_i - D_i}{m_i}\cos(\gamma_i)\cos(\chi_i) - g\check{n}_i(\sin(\gamma_i)\cos(\chi_i)\cos(\check{\phi}_i) + \sin(\chi_i)\cos(\check{\phi}_i)), \\ u_2(t) &= \frac{\check{T}_i - D_i}{m_i}\cos(\gamma_i)\sin(\chi_i) + g\check{n}_i(\cos(\chi_i)\sin(\check{\phi}_i) - \sin(\gamma_i)\sin(\chi_i)\cos(\check{\phi}_i), \\ u_3(t) &= -\left(\frac{\check{T}_i - D_i}{m_i}\sin(\gamma_i) + g\check{n}_i\cos(\gamma_i)\cos(\check{\phi}_i) + g\right). \end{aligned} \tag{38}$$

To utilize the controller given in (36) following this new approach, we replace (32) with (3), (37) and (38) to obtain $u(t)$ from $u_d(t)$. We can then use $u(t)$ from $u_d(t)$ in (35) as required by the control dynamics (34).

We would like to comment on the dependencies within the controlled system. Note that the two underlying factors used to compute the error dynamics are (i) the movement of the leader, and (ii) the movement of the desired point along the ring (controlled using the variables $\varphi(t)$, $\dot{\varphi}(t)$, and $\ddot{\varphi}(t)$). Since the leader moves arbitrarily, given that system (1) operates with wingman control input (36), the true control signal changes from u_w to the angle feedback $\varphi(t)$ introduced to the system via (7). To provide information for $\dot{\phi}(t)$ and $\ddot{\phi}(t)$, we implement control dynamics, defined as

$$\begin{aligned} \dot{\varphi}(t) &= \int \ddot{\varphi}(t)dt, \\ \ddot{\varphi}(t) &= u(t), \end{aligned} \tag{39}$$

where $u(t)$ is the acceleration of the ring angle used to define the wingman's desired position. In addition to providing the feedback information needed in (36), another benefit of (39) is that it provides a continuous profile for the desired position along the ring structure, providing a smooth flight path. The state vector z_{opt}, control vector u_{opt} and differential state vector $\dot{z}_{opt}$ for the optimization problem are represented as

$$z_{opt} = [z_w, \varphi, \dot{\varphi}, \xi] \in \mathbb{R}^{11x1}, \tag{40}$$

$$u_{opt} = [\ddot{\varphi}] \in \mathbb{R}^{1x1}, \tag{41}$$

$$\dot{z}_{opt} = [\dot{z}_w, \dot{\varphi}, \ddot{\varphi}, \dot{\xi}] \in \mathbb{R}^{11x1}. \tag{42}$$

We now define the thrust optimization problem using the controller presented in (36) as

$$\begin{aligned} &\min_{\ddot{\varphi}(t)} \int_{t_o}^{t_f} T_w(\tau) d\tau, \\ &\text{s.t.} \qquad -0.1 < \ddot{\varphi} < 0.1, \end{aligned} \tag{43}$$

subject to (42) where $T_w(t)$ is the thrust defined in (3). Different from case A and case B, the control used for case C ensures convergence to any point on the ring and hence case C does not require any path constraint for optimization. For each optimization problem, the initial state vector z_{opt} is fixed and the final optimization state is left unconstrained. For all optimization problems that we consider in this paper, the initial time and final time are both constrained to a fixed value. This allows us to define our optimization problems as fixed-time, free final-state optimization problems.

D. Optimization Procedure

We have considered three cases of the system structure and described the differences in their optimization problems. Each optimization problem requires *guess* data as an initial guess for finding the solution. Our procedure for procuring the *guess* data uses either approximated or generalized functions instead of the raw state information obtained from simulating system (1). The *guess* data is comprised of the wingman's state information and is generated by the optimizer with respect to said functions. Here, we describe how the generalized functions are used to represent the system state information and generate the *guess* data needed for finding the optimized solution.

1. Approximating the Leader's States

The state vectors used in our optimization problems do not include the leader's state or control information. This is because the optimizer adjusts the state values to find the solution, and we cannot change the leader's information in any practical manner (recall that the leader controls are arbitrarily given). Therefore, another method for obtaining the leader's state and control information is proposed. A simple way to obtain a function approximation is to limit the leader's maneuvers to very simple cases. By limiting the maneuvers, we no longer approximate the function, but can generalize the leader's state as a function of time. Consider the particular cases where a vehicle $i \in \{l, w\}$ performs a steady-state, level-flight bank angle maneuver. The state variable approximation may be obtained using a generalized formulation of the maneuver. In these special case maneuvers, we assume: (i) the vehicle has level flight (*i.e.* constant height h_i), (ii) the speed V_i, load factor n_i and bank angle ϕ_i are held constant, and (iii) the initial state $\mathbf{z}_i(t_o)$ satisfies the steady-state requirements (i) and (ii). Given that these assumptions are met, vehicle i moves with a constant turning rate

$$\omega_i = V_i / R. \tag{44}$$

The controls necessary to perform a uniform circular motion are defined as

$$\begin{aligned} \phi_i(t) &= k_\phi(\phi_d - \phi_i(t)), \\ n_i(t) &= 1/\cot(\phi_i(t)), \\ T_i(t) &= D_i(t), \end{aligned} \tag{45}$$

where ϕ_d is the desired bank angle of vehicle i. We set $\phi_d = \phi_i(t_o)$ for uniform circular motion. Following the law of uniform circular motion, the radius R_i of the circular trajectory being flown by vehicle i during a constant bank angle maneuver is defined as

$$R_i = \frac{V_i^2(t_o)\cot(\phi_i)}{g}. \tag{46}$$

The generalized functions for vehicle i's state variables for any time t is then given in terms of $\mathbf{z}_i(t_o)$ as

$$x_i(t) = R_i \cos(\theta_{o_i} + \theta_i(t)), \tag{47}$$

$$y_i(t) = -R_i \sin(\theta_{o_i} + \theta_i(t)), \tag{48}$$

$$h_i(t) = h_{o_i}, \tag{49}$$

$$V_i(t) = V_{o_i}, \tag{50}$$

$$\gamma_i(t) = 0, \tag{51}$$

$$\chi_i(t) = \theta_{o_i} + \theta_i(t), \tag{52}$$

$$\theta_i(t) = \omega_i t, \tag{53}$$

where θ_{oi}, h_{oi}, V_{oi} are the initial heading angle, initial altitude and initial velocity respectively. $\theta_i(t)$ represents the angular position of the vehicle in the loiter circle with respect to negative y axis. ω_i and R_i are obtained via (44) and (46), respectively. The expressions (45) - (53) are not only useful for defining the leader's state information, but also can be used to generate the wingman's state information to be used as *guess* data for the optimizer. The process for generating the *guess* data is further described next in next section.

2. Generating Guess Data

The optimization method finds a solution by adjusting the system's state and input information within a solution space. Following the system kinematic constraints, a set of state and input variables are incrementally updated by the optimizer in a direction following the negative gradient of the objective function. The initial optimization begins with an initial solution determined by the *guess* data fed to the optimization algorithm. If there are local minimas within the objective function gradient, then the optimized solution can produce different solutions based on what *guess* data is being used. Hence, the selection and procurement of the *guess* data are key factors to the quality of the solution. For the system described in (1) and optimization problems described in Section III, the *guess* data will reflect the simulated state and control information taken from the wingman. The leader information is not included in the *guess* data because the optimization adjusts each value in the state vector to find the solution, and we are not practically able to change the leader's state information. Therefore, one option to generate the *guess* data for each optimization problem described in Section III is to simulate the leader and wingman dynamics (1) together and extract the wingman's state and control information to use as the *guess* data. This option would require the function approximation method (described in III.D.1) to be used within the optimizer, which is computationally expensive due to refitting and solving the polynomial approximations. The polynomial approximations also carry undesired errors when compared to the true data. Another option for generating the *guess* data is to simulate the wingman with respect to the leader's state information obtained through the generalized formulation of a constant bank angle or straight-line maneuver in level-flight as described in III.D.1.

To generate wingman state information, a decision on the control to use for the wingman is also considered. For wingman control, we present two options. In the first option, the wingman may use the control presented in (45). This control type is only valid when the maneuver of the leader is a constant bank angle or straight-line maneuver in level-flight. Also, when implementing this control option, the initial pose of the wingman is defined such that the maneuver's steady-state conditions are satisfied. In our second option for selecting a wingman control to create the *guess* data, we use the ring structure formation control presented in [24]. Note that we also use this control in our case C optimization problem. Observe that if we use the first wingman control option for generating *guess* data, the wingman dynamics follow the formulation described in equations (44)-(53) (originally used to generalize the leader's state information). Therefore, to obtain *guess* data, we use (44)-(53) with the parameters needed to obtain the desired trajectory (*i.e.*, the trajectory of the desired position taken with respect to the leader's state information). Additionally, we verify that the *guess* data satisfies all constraints and is consistent with the differential vectors expressed in (24), (30), and (42). If poor *guess* data is used, *i.e.*, data that reflects kinematic inconsistencies and/or dissatisfies the path constraints, it is difficult for the optimizer to converge and output an optimal solution.

IV. Simulation

In this section, several simulation studies are conducted to provide optimization results for the fixed-wing leader-follower ring structure formation maneuvers. The results reflect a set of minimal thrust profiles that may be used by the wingman under different operating conditions. Utilizing these thrust profiles allows the wingman to realize a 3D trajectory where its energy consumption is reduced. Two simulations are used to provide the optimization results. In the first simulation, a comparison is made between the results for each of the cases described in Section III. In the second simulation, we use only the case A structure of the optimization problem and compare the results for different initial positions of the wingman along the ring structure (*e.g.*, the top-side, left-side, right-side, and bottom-side of the ring structure). The optimization is performed using *OptimTraj* [27] MATLAB library developed by Mathew Kelly for continuous time trajectory optimization. The optimization method used is the *trapezoidal* collocation method. For each optimization problem, the total time and initial state of the trajectory to be optimized are fixed with the final state being free. An in-depth description for the *OptimTraj* library optimization method and algorithm procedure is available in [28] and [29].

We utilize the same optimization parameters across all simulations. These parameters include the *trapezoidal* method's number of grid points (=64), simulation time (=132 seconds), and sampling rate (=0.05 seconds/sample). This

sampling rate is sufficient in identifying convergence properties for the wingman's position on the ring structure. Using these parameters, the computational cost for obtaining convergence is 700-1500 iterations of optimization processed in approximately 15-20 minutes on i-7 16 GB RAM PC. In addition to the optimization parameters, we also use the same maneuver parameters across all simulations. For each simulation, the leader performs a positive, constant bank angle maneuver in level-flight (*i.e.*, loiter maneuver). For our model, we configure the simulation parameters to match the physical properties of a Cessna 172 Skyhawk. The ring structure formation is defined using the radius $R = 10$ m and *center* vector $C = [-10, 0, 0]'$. The leader is set to follow a constant 30° positive bank with a velocity of 60 m/s. Under these conditions, the radius and steady-state angular rate for the leader's trajectory are 635.61 m and 0.0944 rad/s, respectively. The other simulation parameters and initial conditions that are used in each simulation can be found in Table 1.

Table 1 Simulation Parameters

Parameter	Value	Description
m	$1111kg$	Aircraft mass
ρ	$1.225kg/m^3$	Air Density
g	$9.81m/s^2$	Acceleration Due to Gravity
AR	7.32	Wing Aspect Ratio
A_i	$16.2m^2$	Wing Surface Area
e	0.85	Oswald's efficiency parameter
$[k_1, k_2, k_3]$	$[1, 8.5462, 8.170]$	Controller Gains
$[\bar{T}_w, \bar{n}_w, \bar{\phi}_w]$	$[800, 2, \pi/3]$	Modified saturation constraints
$C_{d_{o_i}}$	0.01	Aircraft Parasitic Drag Constant
$[x_o^L, h_o^L, h_o^L]$	[0 m,-635 m,1000 m]	Leader's Initial Position
$[V_o^L, \gamma_o^L, \chi_o^L]$	[60 m/s, 0 rad,0 rad]	Leader's Initial State

A. Comparison Between Different Case Structures

In our first simulation, we show how limited availability of the system control variables affects the performance of the wingman by solving the three optimization problems described in Section III. In order to compare the results from each optimization problem with one another, the initial position of the wingman is set to be the same across all simulations. In particular, the initial position of the wingman is set to be the point along the ring structure located above the leader (*i.e.*, with respect to Figure 1 it is the top-side of the ring structure associated with the ring angle $\varphi = -\pi/2$). This maps the initial location of the wingman to be $[x_o^W, h_o^W, h_o^W] = [-10\text{ m}, -635\text{ m}, 1010\text{ m}]$ and we set $[V_o^W, \gamma_o^W, \chi_o^W] = [60\text{ m/s}, 0\text{ rad}, 0\text{ rad}]$. Results comparing the thrust, desired ring angle, and tracking error between the *guess* data and the optimal solution for the different cases are shown in Figures 3(a), where the tracking error is defined as the absolute distance between the wingman and the desired position on the ring. An energy metric, represented by the total thrust spent, is obtained by integrating the thrust profiles with respect to time. Results comparing the wingman's total thrust spent between the *guess* data and the different cases are shown in Table 2.

Table 2 Energy Comparison Between Different Case Structures

Structure	Wingman's Total Thrust Consumption (N)
Case A	1.45×10^6
Case B	1.54×10^6
Case C	1.43×10^6
Guess Data	1.55×10^6

The *guess* data is generated using a constant angle for the desired position on the ring structure. The constant angle is set to $\varphi = -\pi/2$ such that desired position of the wingman stays on the top of the leader's circular trajectory. To

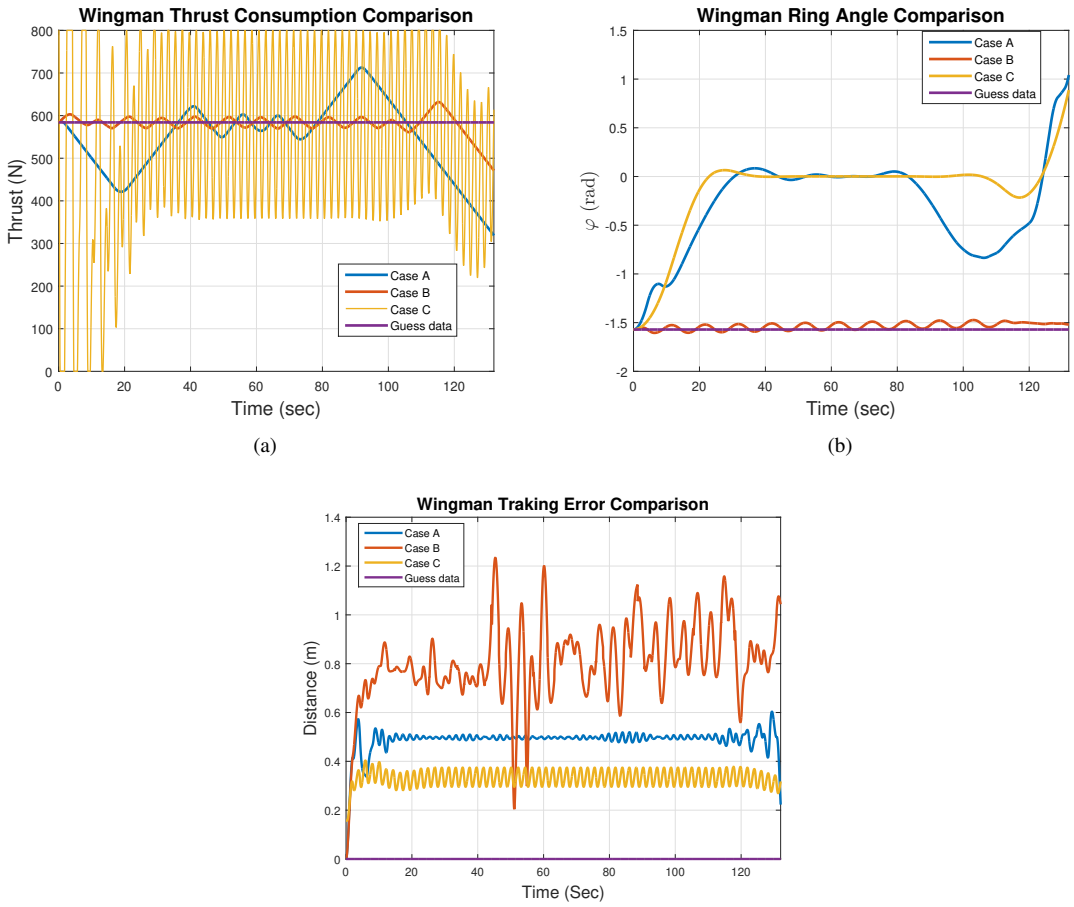

Fig. 3 Figure (a) shows a comparison of the wingman's thrust consumption. Figure (b) shows a comparison of the ring angle information for the position. Figure (c) shows comparison of the tracking error. The tracking error is defined as the absolute distance between the wingman and the desired position on the ring. The comparison is between the *guess* data and cases A, B, and C described in Section III.

maintain this formation when performing the leader-follower maneuver, the wingman travels with a circular trajectory at a same radius as the leader's circular trajectory. Also, in order to maintain this desired formation, the wingman must operate at the same velocity as the leader. Hence, for the *guess* data, holding the desired position requires the wingman use a thrust profile that is the same as the leader's.

Case A offers the best solution in terms of a smooth thrust profile, but suffers from high deviations of the thrust range throughout the maneuver. This is due to the fact that the case A structure has the least restrictive structure out of the three cases. Recall that all available control variables $[\dot{T}_w, \dot{n}_w, \dot{\phi}_w, \ddot{\varphi}]$ are included in the optimization's control vector for case A. The tracking error for the case A solution is also stable and within an acceptable range. One critical issue resulting from the case A solution is that the thrust and ring angle profiles have large deviations (as shown in Figures 3(a) and 3(b)). Case B is structured to have the variables $[\dot{T}_w, \dot{n}_w, \dot{\phi}_w]$ in the optimization's control vector, where the ring angle is defined in terms of the wingman's position. In contrast to case A, case B thrust profile for the wingman has smaller deviations, but still with low frequency oscillations. The position on the ring profile for case B has oscillations due to the dynamics of the differential vector, but slowly moves towards a more energy efficient position. The tracking error for the case B solution has the highest deviations among all cases, while still maintaining the amplitude within an acceptable tolerance. In case C, the optimization control vector is $[\ddot{\varphi}]$. From Table 2, we observe that the case C structure provides the lowest energy consumption, while requiring the maneuver use a highly oscillatory thrust profile. The thrust profile for case C contains high frequency oscillations due to the internal ring structure controller taken from

[24]. The position on the ring profile for case C is similar to case A, where a $\varphi = 0$ ring angle is held for a majority of the flight. This is intuitive, because the ring angle $\varphi = 0$ is the position of the ring associated with the lowest velocity. Hence, maintaining the $\varphi = 0$ position will achieve the minimal thrust profile by reducing the velocity needed to stay in formation. In all cases, the wingman remains in the vicinity of 2 m of the ring as shown in Figure 3(c).

B. Comparison Between Different Initial Wingman Positions Along Ring Structure

In our first simulation, we observed that, from the three optimization problems, case A structure generated the smoothest thrust profiles for executing the leader-follower maneuver. In our second simulation, case A is further analyzed using different initial positions of the wingman along the ring structure. Figure 4 shows the optimal trajectories obtained for one full lap of the leader along its loiter trajectory. Note that the plotted trajectories reflect only a portion of the entire data that makes up the results (recall that two full laps of the loiter maneuver are simulated in a 132 second duration). Results comparing the thrust, desired ring angle, and tracking error between different initial wingman positions along the ring structure are shown in Figures 5(a), 5(b) and 5(c).

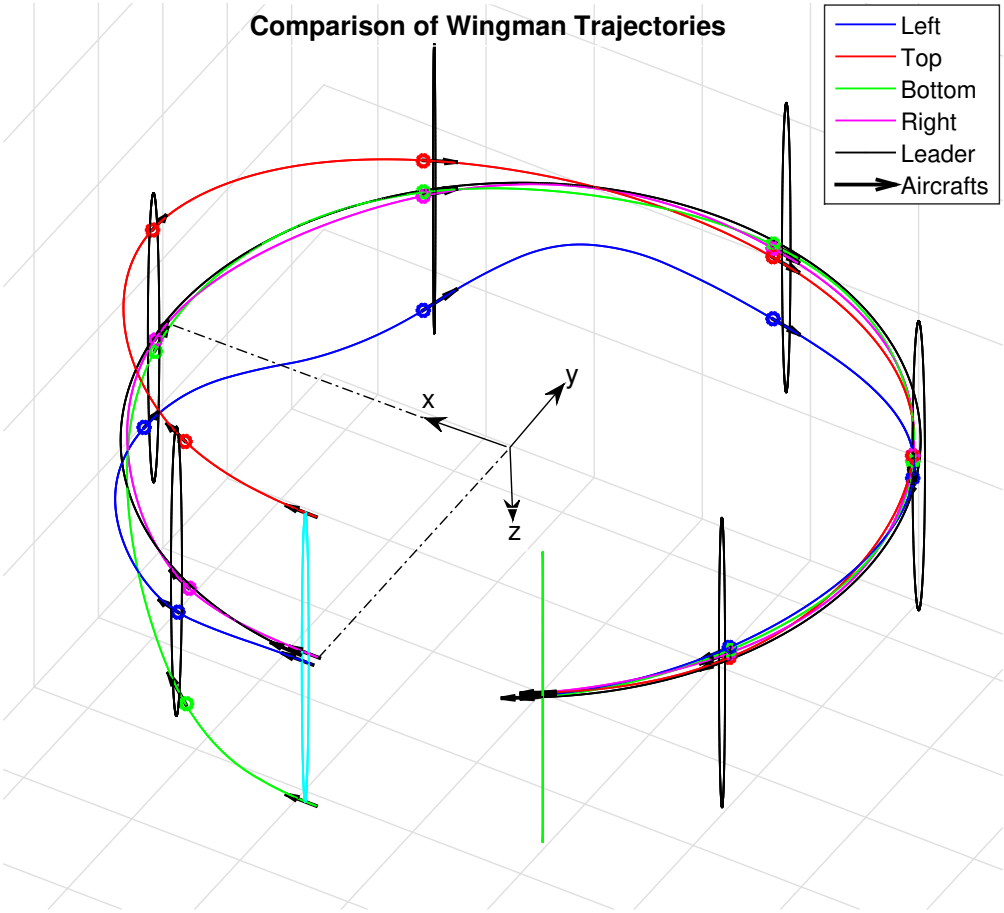

Fig. 4 The image shows the optimized wingman trajectories for one full loiter circle, initially starting at different points in the ring. Initial conditions ($\varphi = 0, \pi/2, \pi$ and $-\pi/2$ corresponding to Right, Top, Left and Bottom positions on the ring, respectively and are shown using different colors). The cyan and green colored rings show the starting and ending points of the maneuvers respectively. The black colored rings are the intermediate points at different time. Black colored arrows represent aircraft position at different time.

We have chosen a large simulation time to find the steady-state value for the optimal position on the ring structure. Doing so allows us to identify three regions in the control profiles, where the different convergence characteristics exist due to the optimization's time constraints. These regions, referred to as regions I, II, and III, are shown in Figures 5(a) and 5(b). In region I, the wingman tries to reach an energy optimal position on the ring structure. This energy optimal

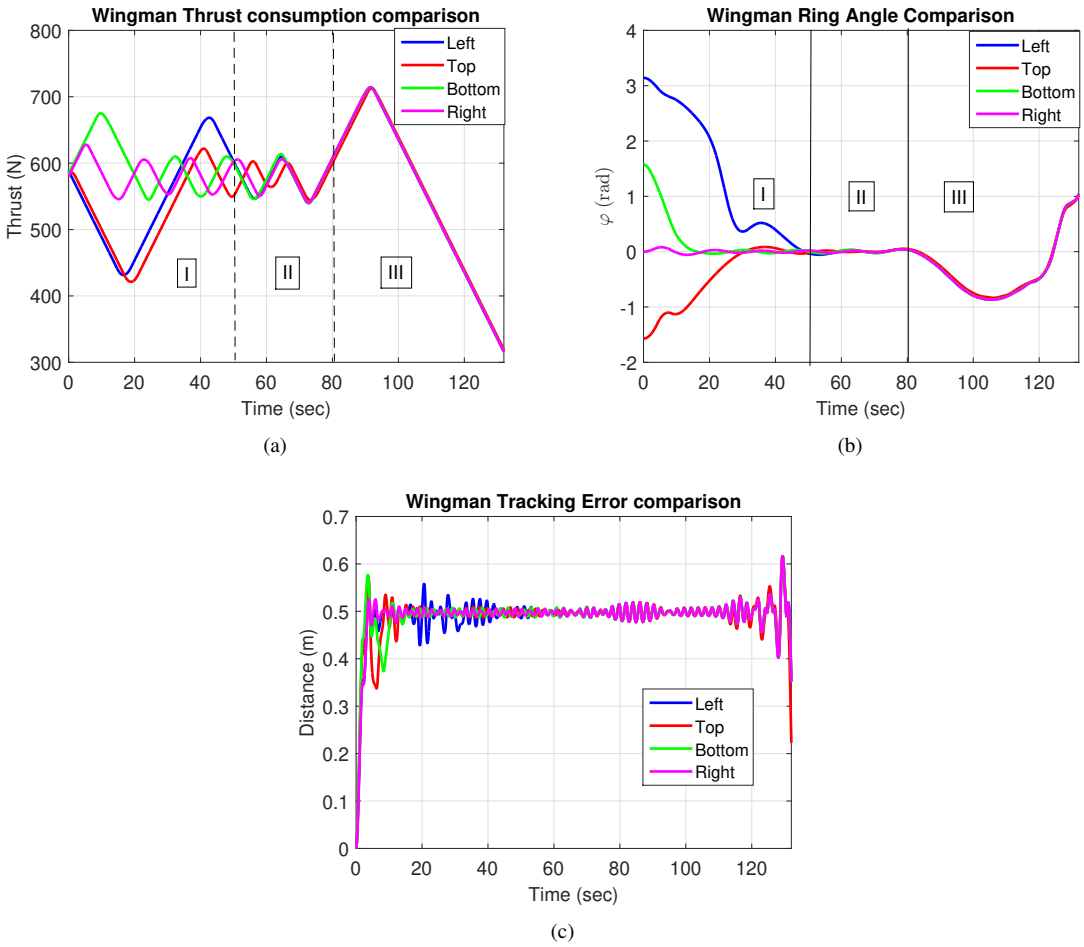

Fig. 5 Figure (a) compares thrust spent by wingman. Figure (b) compares the position on the ring of the wingman. Figure (c) compares the tracking error of wingman starting initially at different points on the ring. Three different intervals of time have been clearly indicated in Figures (a) and (b).

position is the innermost point ($\varphi = 0$) with reference to the leader's circular trajectory. The radius associated with the circular trajectory for this point has a smaller radius than the leader's trajectory, enabling the wingman to travel with a lower velocity and spend less energy. In region II, the wingman tries to maintain its position at the energy optimal point of the ring structure ($\varphi = 0$). In region III, the optimization algorithm finds a solution that increases the wingman's controls in such a way that the potential energy of the vehicle is increased. Note that reducing the total simulation time does not allow the convergence to occur, which implies that the three different regions and convergence of the angle on the ring would not be observable. Also, we note that increasing the simulation time increases the duration of region II. We can see from Figure 5(c) that the ring formation is maintained well and the wingman remains within a vicinity of 0.6 meter of the ring. Although starting from different initial positions on the ring structure, the ring angle converges to the same trajectories within one lap of the loiter trajectory. This shows that the initial position of the wingman does not affect the steady-state value of the angle on the ring for the loiter maneuver. We also observe that different initial conditions affect the time of convergence to the value of the steady-state angle, which is proportional to the angular difference between the steady-state angle and the angle defined by the initial condition.

V. Conclusion

In this paper, we presented three methods to optimize the trajectory of a wingman following a leader-follower ring structure formation. The trajectory is optimized such that the wingman's thrust is minimized and the tracking error is

constrained. By minimizing the thrust, we are able to minimize the energy consumption of the wingman. To solve the issue, we created three different optimization problems by changing the system input structure, and referred them as cases A, B and C. In case A, the optimization problem finds the solution for the wingman controls and the desired position on the ring structure. In case B, the optimization problem finds the solution only for the wingman controls. In case C, the optimization problem finds the solution only for the desired position on the ring structure. To eliminate the need for computing solutions for the wingman controls in case C, an existing ring structure control method is employed. The optimized trajectory was obtained by taking the results from any case structure (A, B, or C) and implementing the corresponding wingman controls and desired ring angle information. To supplement the optimization problems, we also included a description of the procedure for creating the *guess* data used to initialize the optimization algorithm. Our studies show that: (i) Smooth thrust profiles are achievable solutions by including thrust in the optimization objective function and controlling the derivatives of control inputs whose values are bounded to small finite values, and (ii) in a normally constrained system performing constant bank angle maneuvers, where the wingman controls and desired position on ring structure are available as system inputs (case A), the trajectories for different initial positions of the wingman along the ring will converge. The point that they converge to is the inside of the ring, *i.e.*, the point on the ring structure associated with the lowest velocity. We will incorporate these findings in our future work to generate energy-efficient aircraft maneuvers in more practical and complex environments. We are also interested in extending our optimization procedure by evaluating different settings of optimization constraints and parameters to obtain the best optimal solution.

References

[1] Avellar, G. S., Pereira, G. A., Pimenta, L. C., and Iscold, P., "Multi-UAV Routing for Area Coverage and Remote Sensing with Minimum Time," *Sensors*, Vol. 15, No. 11, 2015, pp. 27783–27803.

[2] Azari, M. M., Rosas, F., Chen, K.-C., and Pollin, S., "Ultra Reliable UAV Communication Using Altitude and Cooperation Diversity," *IEEE Transactions on Communications*, Vol. 66, No. 1, 2017, pp. 330–344.

[3] Mirzaeinia, A., Hassanalian, M., Lee, K., and Mirzaeinia, M., "Energy Conservation of V-Shaped Swarming Fixed-Wing Drones Through Position Reconfiguration," *Aerospace Science and Technology*, Vol. 94, 2019, p. 105398.

[4] Zhang, J., and Yan, J., "A Novel Control Approach for Flight-Stability of Fixed-Wing UAV Formation With Wind Field," *IEEE Systems Journal*, 2020.

[5] Rabelo, M. F. S., Brandao, A. S., and Sarcinelli-Filho, M., "Landing a UAV on Static or Moving Platforms using a Formation Controller," *IEEE Systems Journal*, 2020.

[6] Zhang, J., Yan, J., and Zhang, P., "Multi-UAV Formation Control Based on a Novel Back-Stepping Approach," *IEEE Transactions on Vehicular Technology*, Vol. 69, No. 3, 2020, pp. 2437–2448.

[7] Zhu, X., Liang, Y., and Yan, M., "A Flexible Collision Avoidance Strategy for the Formation of Multiple Unmanned Aerial Vehicles," *IEEE Access*, Vol. 7, 2019, pp. 140743–140754.

[8] Zhao, Y., Jiao, L., Zhou, R., and Zhang, J., "UAV Formation Control with Obstacle Avoidance Using Improved Artificial Potential Fields," *36th Chinese Control Conference*, 2017, pp. 6219–6224.

[9] Zhang, J., Yan, J., and Zhang, P., "Fixed-Wing UAV Formation Control Design with Collision Avoidance Based on An Improved Artificial Potential Field," *IEEE Access*, Vol. 6, 2018, pp. 78342–78351.

[10] Zhang, J., Yan, J., Zhang, P., and Kong, X., "Collision Avoidance in Fixed-Wing UAV Formation Flight Based on a Consensus Control Algorithm," *IEEE Access*, Vol. 6, 2018, pp. 43672–43682.

[11] Shao, Z., Yan, F., Zhou, Z., and Zhu, X., "Path Planning for Multi-UAV Formation Rendezvous Based on Distributed Cooperative Particle Swarm Optimization," *Applied Sciences*, Vol. 9, No. 13, 2019, p. 2621.

[12] Shao, S., Peng, Y., He, C., and Du, Y., "Efficient Path Planning for UAV Formation via Comprehensively Improved Particle Swarm Optimization," *ISA Transactions*, Vol. 97, 2020, pp. 415–430.

[13] Zhu, X., Zhang, X.-x., Qu, Y.-h., et al., "Consensus-Based Three-Dimensional Multi-UAV Formation Control Strategy with High Precision," *Frontiers of Information Technology & Electronic Engineering*, Vol. 18, No. 7, 2017, pp. 968–977.

[14] Zhang, B., Sun, X., Liu, S., and Deng, X., "Adaptive Model Predictive Control with Extended State Observer for Multi-UAV Formation Flight," *International Journal of Adaptive Control and Signal Processing*, Vol. 34, No. 10, 2020, pp. 1341–1358.

[15] Kartal, Y., Subbarao, K., Gans, N. R., Dogan, A., and Lewis, F., "Distributed Backstepping Based Control of Multiple UAV Formation Flight Subject to Time Delays," *IET Control Theory & Applications*, Vol. 14, No. 12, 2020, pp. 1628–1638.

[16] Guo, K., Li, X., and Xie, L., "Ultra-Wideband and Odometry-Based Cooperative Relative Localization with Application to Multi-UAV Formation Control," *IEEE Transactions on Cybernetics*, Vol. 50, No. 6, 2019, pp. 2590–2603.

[17] Milutinović, D., and Casbeer, D. W., "Leader-Follower Formation Feedback Control Composed of Turning Rate and Velocity Controllers," *International Conference on Unmanned Aircraft Systems*, 2020, pp. 1189–1198.

[18] Pachter, M., D'Azzo, J. J., and Dargan, J., "Automatic Formation Flight Control," *Journal of Guidance, Control, and Dynamics*, Vol. 17, No. 6, 1994, pp. 1380–1383.

[19] Pachter, M., D'Azzo, J. J., and Proud, A. W., "Tight Formation Flight Control," *Journal of Guidance, Control, and Dynamics*, Vol. 24, No. 2, 2001, pp. 246–254.

[20] Barfoot, T. D., and Clark, C. M., "Motion Planning for Formations of Mobile Robots," *Robotics and Autonomous Systems*, Vol. 46, No. 2, 2004, pp. 65–78.

[21] Low, C. B., and San Ng, Q., "A Flexible Virtual Structure Formation Keeping Control for Fixed-Wing UAVs," *IEEE International Conference on Control and Automation*, 2011, pp. 621–626.

[22] Low, C. B., "A Rapid Incremental Motion Planner for Flexible Formation Control of Fixed-Wing UAVs," *IEEE Conference on Decision and Control*, 2012, pp. 2427–2432.

[23] Kownacki, C., and Ambroziak, L., "Flexible Structure Control Scheme of a UAVs Formation to Improve the Formation Stability During Maneuvers," *Acta Mechanica et Automatica*, Vol. 11, No. 3, 2017, pp. 178–185.

[24] Tran, D. M., Casbeer, D., Garcia, E., Weintraub, I. E., Milutinovic, D., and Manyam, S. G., "Ring Formation Maneuver: Single-Integrator Kinematics," *AIAA Scitech 2021 Forum*, 2021, p. 0978.

[25] Menon, P., "Short-Range Nonlinear Feedback Strategies for Aircraft Pursuit-Evasion," *Journal of Guidance, Control, and Dynamics*, Vol. 12, No. 1, 1989, pp. 27–32.

[26] Anderson, J. D., *Introduction to Flight*, McGraw-Hill Higher Education, 2005.

[27] Kelly, M., "An Introduction to Trajectory Optimization: How To Do Your Own Direct Collocation," *SIAM Review*, Vol. 59, No. 4, 2017, pp. 849–904.

[28] Kelly, M. P., *OptimTraj User's Guide, Version 1.5*, wiki, 2019.

[29] Betts, J. T., *Practical Methods for Optimal Control and Estimation Using Nonlinear Programming*, SIAM, 2010.